

Structure Functions in Stratified Shear Turbulence

Joseph Werne* and David C. Fritts
Colorado Research Associates
Boulder, CO 80301

Abstract

Shear turbulence induced by the Kelvin-Helmholtz (KH) instability in a stratified fluid is simulated in support of the AirBorne Laser (ABL) project using the DoD Cray T3E's at CEWES and NAVO. Analysis of the resulting turbulent flow is carried out via decompositions into horizontal-mean, spanwise-averaged, and fluctuating components. Transport, production and dissipation terms are evaluated for each of the flow components as functions of the vertical direction and time. Fits are obtained for second-order structure functions in streamwise and spanwise directions, allowing us to obtain structure-function coefficients and power-law exponents as well as the turbulence inner length scale for all of the flow fields. Our main results are: 1) temperature fluctuations are nearly stationary in the middle of the shear layer where mixing is vigorous, while the entrainment zones at the layer's edges are non-stationary throughout the layer's evolution; 2) velocity fluctuations are non-stationary in the middle of the shear layer for as long as the primary KH vortex is active (≈ 6 buoyancy periods); 3) temperature structure-function power-law exponents concentrate between the theoretical values of $\alpha = 2/5$ and $2/3$ for stratified and unstratified turbulence, respectively; however, 4) exponents for the longitudinal and transverse velocity structure functions also tend between $\alpha = 2/5$ and $2/3$ (or assume even lower values for some velocity components and directions), despite the larger theoretical prediction for strongly stratified flow ($\alpha = 6/5$); 5) structure-function coefficients for the streamwise, spanwise and vertical velocity components obtained in the middle of the turbulent shear layer are consistent with so-called "universal constants" of $C = 2.1$, 1.6 and 0.9 , respectively (note, the Kolmogorov constant C_1 is related to C via $C_1 \approx 0.76C$); 6) the equivalent universal constant for the temperature field C_θ is found to be consistent with $C_\theta = 3.3$; and 6) estimates of the turbulence inner scale from the temperature structure function are consistent with $\ell_o \approx 7.4\ell_K$, where ℓ_K is the Kolmogorov length scale. Coefficients obtained from velocity structure functions are larger than 7.4 . These results, combined with in-situ balloon, tethered kite, and remote radar backscatter measurements, will be used by Dr. Bill Brown to refine the turbulence phase screens needed to conduct ABL optical propagation simulations.

Introduction

The main objective of the ABL program is to develop adaptive optical systems capable of focusing laser energy on a target through a few hundred kilometers horizontally in the upper troposphere and lower stratosphere. Two facets of the ABL program are currently being carried out with the aid of HPCMO Challenge allocations: optical propagation simulations through modeled stratospheric turbulence directed by Dr. Bill Brown address the design issues associated with the ABL optical system; our companion effort concentrates on improving the understanding of stratospheric turbulence phenomena so that more realistic

models may be used for atmospheric-propagation-simulation input. In this report we concentrate on characterizing turbulence induced by wind shear. Future and continuing work will address turbulence resulting from breaking gravity waves.

Atmospheric Turbulence

Turbulence in the lower stratosphere and upper troposphere, where ABL will operate, is spatially and temporally complex. Single balloon ascensions from the ground to above the tropopause typically report 10 to 20 well-defined turbulent layers, in various states of activity, which range from 100 m to 1 km in depth (Coulman et al. 1995). Successive balloon launches give some idea about the temporal variability, with intense mixing occurring over roughly an hour and evidence of previously active mixing layers existing for up to a few days (Ierkic et al. 1990, Coulman et al. 1995). In addition, radar backscatter measurements of turbulent layers that drift with the horizontal mean flow give an indication of horizontal spatial coherence: Events containing $O(10)$ KH vortices (or billows) of roughly 5 km wavelengths have been observed, indicating horizontal coherence over as much as 50 km (Rüster and Klostermeyer 1983, Chilson et al. 1997).

Stable density stratification throughout the atmosphere is responsible for both the layering of turbulence with height and its episodic nature. In addition, wind shear and/or a source of large-amplitude gravity waves (e.g., flow over complex topography) is needed to instigate turbulence in the stably stratified atmosphere. Hence, large-scale anisotropy and non-stationarity are necessarily components of atmospheric turbulence, and therefore modification to homogeneous and isotropic turbulence theory is required. Characterizing time-evolving inhomogeneous and anisotropic turbulence through canonical instability processes relevant to atmospheric turbulence is the focus of this work. Our current results must be combined with 1-D observational (e.g., balloon, kite, and radar) information to develop an understanding of the spatial and temporal structure of turbulence along 100 km paths through the atmosphere. In addition, improved characterization resulting from this work of atmospheric turbulence at small spatial scale could be used to improve sub-grid models in meso-scale simulations, so that atmospheric turbulence forecasts might be made.

Problem Formulation

In order to study turbulence in stratified environments, two canonical instability processes that give rise to turbulence are currently under study: shear instability and gravity-wave breaking. Here we report our results for shear flow.

Instability is initiated by exciting the most-unstable asymptotic linear eigenmode for an initial hyperbolic-tangent shear profile $U = U_o \tanh(z/h)$ and linear temperature $T = \beta z$. U_o , h and β are the maximum initial flow velocity, half of the initial shear-layer depth, and the background temperature gradient, respectively. Small-amplitude noise is also added to the initial condition so that 3D flow structures may develop.

Solutions are obtained in a horizontally periodic domain contained by stress-free top and bottom boundaries by time-integrating the Fourier coefficients of the spectrally represented flow fields. The basic progression is 1) growth of the initial eigenmode to a well-defined, large-amplitude, non-linear vortex, to 2) development of streamwise aligned vortex-tube structures when the primary KH vortex overturns and develops local regions of unstable

stratification, to 3) erosion of the KH vortex and modification of the background mean by small-scale turbulence. The numerical method, basic evolution of the shear layer, and code performance have been documented elsewhere (Werne and Fritts 1998, 1999a,b; Werne et al. 2000a,b). Here we describe analysis of the resulting turbulent layer as it evolves from and coexists with the primary vortex.

Flow Decomposition

To facilitate analysis of the turbulence and KH vortex, we employ the decomposition $T = \bar{T} + \tilde{T} + T'$, where T is the 3D temperature field, \bar{T} is the horizontal spatial average of T , and \tilde{T} is the spanwise average of $T - \bar{T}$. Note that we also use the notation $\langle T \rangle = \bar{T}$. An identical decomposition is used for the velocity field.

Because the primary vortex is initially two dimensional, we suggest \tilde{T} represents the temperature of the evolving KH billow. \bar{T} represents the evolving mean. T' is the remainder, which we interpret as small-scale fluctuations. We caution the reader that \tilde{T} is only a rough guide to the temperature associated with billow dynamics because 1) the evolving billow can (and does) possess 3D features, and 2) other contributions to \tilde{T} besides the KH billow are possible (e.g., turbulent entrainment at the edges of the shear layer). Despite these difficulties, the mathematical decomposition $T = \bar{T} + \tilde{T} + T'$ can be carried out in a straightforward manner, and potential- and kinetic-energy (PE and KE) evolution equations for each component can be derived. In the interest of brevity, we present only the PE evolution equations below.

$$\begin{aligned} \partial_i \bar{T}^2 / 2 &= -\partial_j \left(\overline{U_j \bar{T}^2} / 2 + \overline{\tilde{U}_j \tilde{T} \bar{T}} + \overline{U'_j T' \bar{T}} - Pe^{-1} \partial_j \bar{T}^2 / 2 \right) \\ &\quad + \overline{\tilde{U}_j \tilde{T} \partial_j \bar{T}} + \overline{U'_j T' \partial_j \bar{T}} - Pe^{-1} \overline{\partial_j \bar{T} \partial_j \bar{T}} \end{aligned} \quad (1)$$

$$\begin{aligned} \partial_i \tilde{T} \tilde{T} / 2 &= -\partial_j \left(\overline{U_j \tilde{T} \tilde{T}} / 2 + \overline{\tilde{U}_j \tilde{T} \tilde{T}} / 2 + \overline{U'_j T' \tilde{T}} - Pe^{-1} \partial_j \tilde{T} \tilde{T} / 2 \right) \\ &\quad + \overline{U'_j T' \partial_j \tilde{T}} - \overline{\tilde{U}_j \tilde{T} \partial_j \bar{T}} - Pe^{-1} \overline{\partial_j \tilde{T} \partial_j \tilde{T}} \end{aligned} \quad (2)$$

$$\begin{aligned} \partial_i \bar{T} T' / 2 &= -\partial_j \left(\overline{U_j \bar{T} T'} / 2 + \overline{\tilde{U}_j \tilde{T} T'} / 2 + \overline{U'_j T' T'} - Pe^{-1} \partial_j \bar{T} T' / 2 \right) \\ &\quad - \overline{U'_j T' \partial_j \tilde{T}} - \overline{U'_j T' \partial_j \bar{T}} - Pe^{-1} \overline{\partial_j T' \partial_j T'} \end{aligned} \quad (3)$$

The first set of terms on the right-hand side of each equation represents transport processes. They are divergences of energy flux, and are zero in homogeneous, isotropic flow. Because the problem we study is neither homogeneous nor isotropic, these terms are not zero. The next two terms on the right hand side of each equation are deformation-work (also called production) terms. They quantify transfer between the mean and the fluctuations ($\overline{U'_j T' \partial_j \bar{T}}$), the mean and the spanwise average ($\overline{\tilde{U}_j \tilde{T} \partial_j \bar{T}}$), and the spanwise average and the fluctuations ($\overline{U'_j T' \partial_j \tilde{T}}$). The final term on the right-hand side of each equation is the dissipation term. $Pe = U_o h / \kappa$ is the Peclet number; it is the thermal equivalent of the Reynolds number $Re = U_o h / \nu$. ν and κ are kinematic viscosity and thermal diffusivity. For our highest- Re simulations we set $Re = Pe = 2500$. The actual Reynolds number $Re_L = UL / \nu$ of the turbulent shear layer after it has grown to its final full depth L is roughly $Re_L = 30,000$. Here $U \approx 2U_o$ is the velocity difference across the full shear-layer depth.

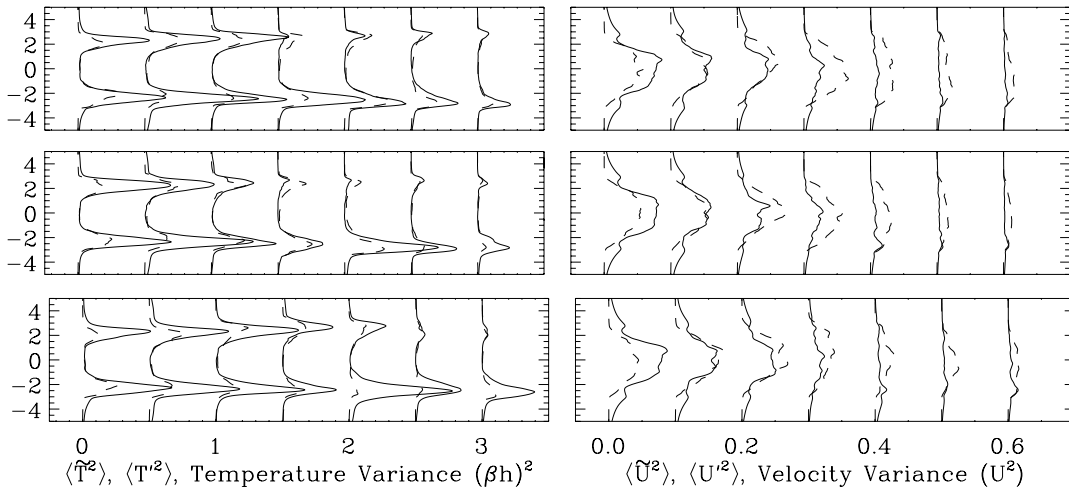


Figure 1: Temperature and velocity variance profiles through simulated stratified shear layers with $Re = 1024$ (lower panel), 2000 (middle panel) and 2500 (upper panel) corresponding to $Re_L \approx 12,000$, 24,000 and 30,000. $\langle \tilde{T}\tilde{T} \rangle$ and $\langle T'T' \rangle$ are indicated by solid and dashed lines, respectively. Similar line styles are used for $\langle \tilde{U}_j\tilde{U}_j \rangle$ and $\langle U'_jU'_j \rangle$. Profiles are shown for $t = 117, 134, 142, 165, 183, 202$ and 220 in units of h/U_o . In the upper troposphere, assuming a 5 minute buoyancy period, $t = 220h/U_o$ corresponds to roughly 40 minutes.

Temperature and Velocity Variance

Fig. 1 shows temperature- and velocity-variance profiles at seven times during the flow evolution after the primary KH vortex has made the transition to 3D morphology. (See previous DoD User Group Meeting papers (Werne and Fritts 1998, 1999) for details of the flow evolution at earlier time.) Results for $Re = 1024$ (bottom), 2000 (middle) and 2500 (top) are presented. Note that despite the differing values of Re in each of the simulations, the mid-layer statistics ($-1.5 < z < 1.5$) are similar in magnitude and shape. This is because the KH eigenmode grows essentially inviscidly and is nonlinearly saturated by density stratification, not viscosity. Hence, for sufficiently large Re , the statistical behavior of the large-scale flow is nearly independent of Re .

The temperature statistics in the edge regions of the shear layer do not exhibit the same degree of Re independence as the layer interior. This is because the edges of the shear layer near $z = \pm 2.5$ are nonstationary and are associated with the rapid evolution of sharp (i.e., small scale) spatial gradients. Hence, we should not expect statistical similarity in the edge regions for different dynamical realizations, even at the same value of Re , let alone at different values.

Mean, Spanwise-Average, and Turbulence Production

Fig. 2 shows profiles for production rates in the top six panels for mean, spanwise-average and fluctuation PE and KE for $Re = 2500$. The lowest two panels depict total fluctuation production and dissipation rates. The figure indicates vigorous exchange between the mean and the 2D billow KE (upper right panel) out to $t = 165$. Similar exchange of PE in the layer edges is evident for all times reported (upper left panel). Rapid variation of the

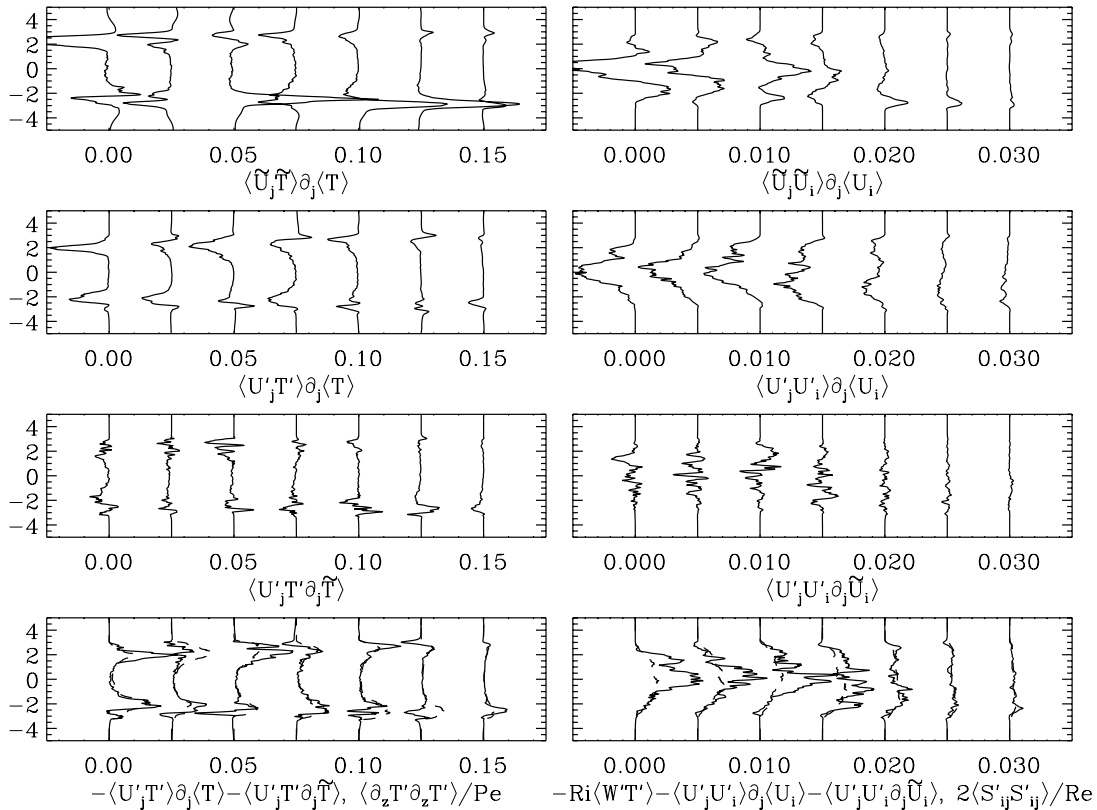


Figure 2: Production and dissipation rates of PE and KE for mean, spanwise average and fluctuations for $Re = 2500$. Top panels show mean-flow production by spanwise-averaged field. The next set of panels depict mean-flow production by fluctuations. The third set shows production of spanwise-average fields by 3D fluctuations. The bottom set superposes the sum of fluctuation production (solid) with fluctuation dissipation (dashed).

large-scale flow caused by mean-flow/spanwise-average interactions prohibits equilibration of turbulence production and dissipation rates (bottom panels) for PE in the layer edges and KE at midlayer. Contributions from gradient transport terms (not shown) indicate redistribution of mean, billow, and fluctuation rates in KE near the middle of the layer for $t < 165$ and in PE near the layer edges for all t . When the primary KH vortex is drained of KE (by $t \approx 174$), midlayer exchange of KE and PE is dominated by erosion of the mean by turbulent fluctuations, and midlayer fluctuation production and dissipation balance. In contrast, the edge-region statistics of the temperature field exhibit persistent interaction among all three components of the flow (mean, spanwise average, and fluctuations), and fluctuation PE production and dissipation do not balance here. This is because the edge regions are associated with persistent entrainment dynamics as turbulent interior fluid punches into outer quiescent fluid. The flow in the edge regions is non-stationary throughout the full course of evolution, and it is clear that a statistical characterization will be most challenging here.

Phase-Screen Construction from Second-Order Structure Functions

ABL optical-propagation simulations employ the so-called phase-screen approximation in which the cumulative effects of atmospheric refractive-index variations are represented by

2D planes that specify random phases for electromagnetic waves propagating normal to the planes. Free-space propagation is computed between the screens. At the screens, the phase of the laser beam is adjusted according to the spatially-dependent value specified by the phase screen.

The form of the second-order structure functions (defined below) of the index-of-refraction field (or, equivalently, the temperature field) must be assumed when generating phase screens for ABL optical propagation simulations (see Brown 1997, 1998, 1999). Currently, phase screens are constructed assuming homogeneous and isotropic turbulence statistics with spatially varying amplitudes that are consistent with observed variations in atmospheric turbulence intensity, either from in-situ balloon or kite measurements or from aircraft data. Since the observations are necessarily limited to 1D paths through complex atmospheric flow fields, only partial information about the 3D structure and time evolution of atmospheric turbulence is directly available from observations. The turbulence simulations reported here offer a 3D characterization of evolving stratified shear turbulence which can be used to augment 1D atmospheric observations. By using both 1D observational and 3D simulation results to refine the specification of temperature structure functions, improved phase screens can be generated for optical propagation work.

Fitting Simulated Structure Functions

The second-order structure function for T is defined by $\Delta_{\vec{r}}T^2 = \langle (T(\vec{x} + \vec{r}) - T(\vec{x}))^2 \rangle$. \vec{r} is the spatial separation of two points in the 3D field, and $\langle \rangle$ indicates averaging over \vec{x} . For $\vec{r} \rightarrow 0$, $\Delta_{\vec{r}}T^2 = \langle (\vec{\nabla}T \cdot \hat{r})^2 \rangle r^2$, where \hat{r} is a unit vector in the \vec{r} direction. For larger spatial separations, the dependence of $\Delta_{\vec{r}}T^2$ on \vec{r} is determined by the spatial statistics of T . For example, if the fluctuations in T are generated by homogeneous/isotropic turbulence, then $\Delta_r T^2 = C_\theta^2 \epsilon^{-1/3} \chi r^{2/3}$ for r in the inertial subrange. Similarly, $\Delta_r U^2 = C \epsilon^{2/3} r^{2/3}$ for the turbulent velocity field U (Monin and Yaglom 1975). C and C_θ are universal constants. $\epsilon = 2\nu \langle s_{ij}s_{ij} \rangle$ and $\chi = \kappa \langle \partial_i T \partial_i T \rangle$ are the viscous and thermal dissipation rates, respectively. $s_{ij} = (\partial_i u_j + \partial_j u_i)/2$ is the strain-rate tensor.

Bolgiano (1959) investigated theoretical spectra for T and U when stable stratification dominates the dynamics (and ϵ is assumed to be unimportant). In this case two different power laws are suggested: $\Delta_r T^2 = C'_\theta Ri^{-2/5} \chi^{4/5} r^{2/5}$ and $\Delta_r U^2 = C' Ri^{4/5} \chi^{2/5} r^{6/5}$. $Ri = g\alpha\beta/(\partial_z U)^2$ is the Richardson number; g , α and $\partial_z U$ are acceleration due to gravity, the thermal expansion coefficient of the fluid and the vertical gradient of horizontal velocity, respectively.

Fig. 3 shows compensated (i.e., divided by r^2) second-order structure functions for T and all velocity components near midlayer obtained from simulations with $Re = 2500$ at $t = 183h/U_o$. U , V and W are the streamwise-, spanwise- and vertical-velocity components, respectively. The horizontal dashed line indicates the measured value of the mean squared horizontal gradient. The sloped dashed line represents a least-squares fit of the structure function to $C_A^2 r^\alpha$ between three times the inner scale ℓ_o and $L_x/4$. Here A in C_A^2 denotes the field being fit (T , U , etc.). Also L_x is the streamwise extent of the simulation domain, and ℓ_o is defined as the intersection point of the r^2 and r^α curves. The values for the fit parameters in the figure are as follows:

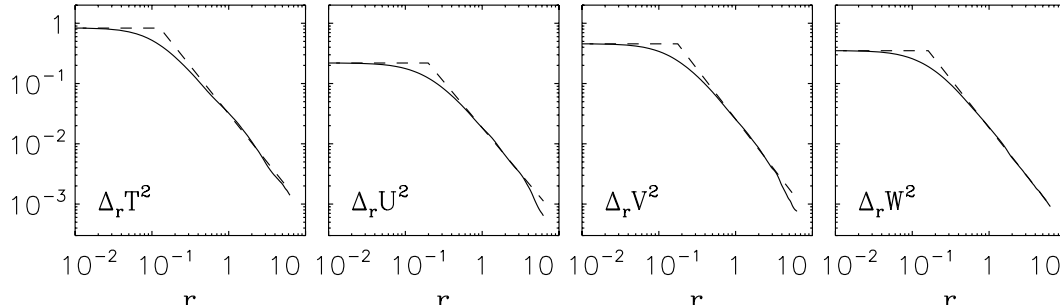


Figure 3: Compensated (i.e., divided by r^2) second-order structure functions for T , U , V and W near midlayer for $Re = 2500$ at $t = 183h/U_o$. The dashed lines indicate the measured value of the mean squared horizontal gradient (horizontal line) and a least-squares fit (slanted line) to $C_A^2 r^\alpha$ between three times the inner scale ℓ_o and $L_z/4$. A denotes the field being fit (e.g., T , U , etc.).

$$\begin{aligned}
 C_T^2 &= 0.031 & \alpha &= 0.40 & \ell_o &= 0.13 \\
 C_U^2 &= 0.018 & \alpha &= 0.47 & \ell_o &= 0.20 \\
 C_V^2 &= 0.025 & \alpha &= 0.34 & \ell_o &= 0.18 \\
 C_W^2 &= 0.018 & \alpha &= 0.38 & \ell_o &= 0.16
 \end{aligned}$$

These values are typical, with α for T and U lying between 0.4 and 0.66, and with α for V and W somewhat smaller. Though this range is consistent with the limiting cases for stratification dominated (Bolgiano 1959) and homogeneous/isotropic turbulence (Kolmogorov 1941) for $\Delta_r T^2$, they are lower than that predicted for $\Delta_r U^2$ and the other velocity components. More work is required to understand this behavior of the simulated flow fields.

Fig. 3 presents results for a single depth in the shear layer at a particular time. However, we can gauge the variation in the fit parameters if we explore the depth and time dependence. Such a study is undertaken in Fig. 4, where profiles of α , C_T^2 and ℓ_o are plotted at seven different times for $Re = 2500$. Panels on the left (right) show results for structure functions computed with streamwise (spanwise) spatial separations r . The top row of panels depicts the exponent α . Predictions for homogeneous/isotropic turbulence (dashed line) and stratification-dominated turbulence (dotted line) are also included. The middle row of panels depicts the coefficient C_T^2 (solid curve). The dashed curve shows the value predicted for homogeneous isotropic flow $C_T^2 \approx C_\theta \epsilon^{-1/3} \chi$ with C_θ set to 3.3. The bottom row shows ℓ_o (solid curve) along with the estimate $C_\ell \ell_K$, where $\ell_K = (\nu^3/\epsilon)^{1/4}$ and C_ℓ is set to 7.4.

Unlike experimental determinations of the parameters involved, ϵ and χ are not estimated, but are directly computed from the 3D simulation fields. As a result, determination of C_θ and C_ℓ is simplified in our case. Our result $C_\theta \approx 3.3$ is consistent with atmospheric measurements of $C_\theta = 3.3 \pm 0.3$ (Kaimal et al. 1972), $C_\theta \approx 3.5$ (Gurvich and Zubkovskii 1966), and $C_\theta \approx 3.3$ (Paquin and Pond 1971). Similarly, $C_\ell \approx 7.4$ is also observed in atmospheric measurements (Hill and Clifford 1978 and references therein). We note that careful observation of Fig. 4 will detect a slightly larger value of ℓ_o from $r = x$ than from $r = y$. This departure from perfect isotropy and the slight increase in streamwise spatial scales relative to spanwise scales

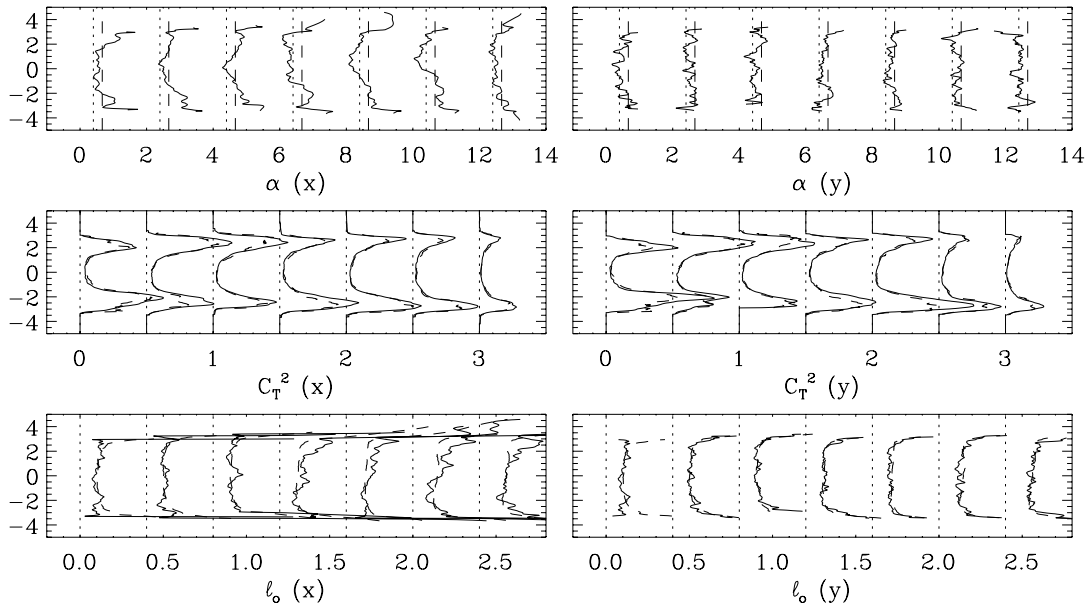


Figure 4: Profiles of temperature structure-function fit parameters at $t = 117, 134, 142, 165, 183, 202$ and 220 in units of h/U_o . Left panels show structure-function fits for streamwise spatial separations r , while right panels show fits for spanwise separations. The top row of panels show α through the shear layer. Dotted and dashed lines indicate $\alpha = 2/5$ and $2/3$, respectively. The middle panel depicts C_T^2 (solid curve). The dashed curve shows $C_T^2 = C_\theta \epsilon^{-1/3} \chi$ predicted by Kolmogorov 1941 theory with C_θ set to 3.3. The bottom panel depicts the measured inner scale ℓ_o (solid curve) along with $7.4(\nu^3/\epsilon)^{1/4}$.

results from the background shear $\langle U(z) \rangle$. Previously, we quantified the magnitude of this departure to be $\langle \partial_y T \partial_y \rangle \approx 1.1 \langle \partial_x T \partial_x T \rangle$, suggesting an increase in the streamwise length scale of $\approx 5\%$ (Werne and Fritts 1999b).

Fig. 5, presents the same profiles as Fig. 4 for the streamwise velocity field. Comparison of C_U^2 and Kolmogorov predictions $C_U^2 = C \epsilon^{2/3}$ for $r = x$ and $C_U^2 = 4/3 C \epsilon^{2/3}$ for $r = y$ are made with C set to 2.1. For $t < 174$, the simulated solutions and predictions for homogeneous/isotropic flow do not agree. Specifically, different values of C are required for streamwise ($r = x$) and spanwise ($r = y$) structure functions. Also, C must vary with height for measured and predicted values of C_U^2 for $r = y$ to agree at $t = 165$. Clearly the non-stationarity of KE for $t < 174$ (see Fig. 2 and associated discussion) complicates the mid-layer dynamics, and simple homogeneous/isotropic arguments cannot be trivially applied. In contrast, once the mean-flow/spanwise-average interaction $\langle \tilde{U}_j \tilde{U}_i \rangle \partial_j \langle U_j \rangle$ subsides after $t = 165$, dissipation balances production for the fluctuations as we've already noted (see Fig. 2), and the longitudinal and transverse structure functions of the streamwise velocity then agree better with predictions for homogeneous/isotropic flow. Furthermore, at these later times, the value we obtain for the universal constant $C \approx 2.1$ is consistent with atmospheric observations: $C \approx 2.0 \pm 0.1$ (Kaimal et al. 1972), $C \approx 2.1 \pm 0.2$ (Wyngaard and Coté 1971), $C \approx 2.1 \pm 0.1$ (Wyngaard and Pao 1971), and $C \approx 2.1$ (Gibson 1962, 1963).

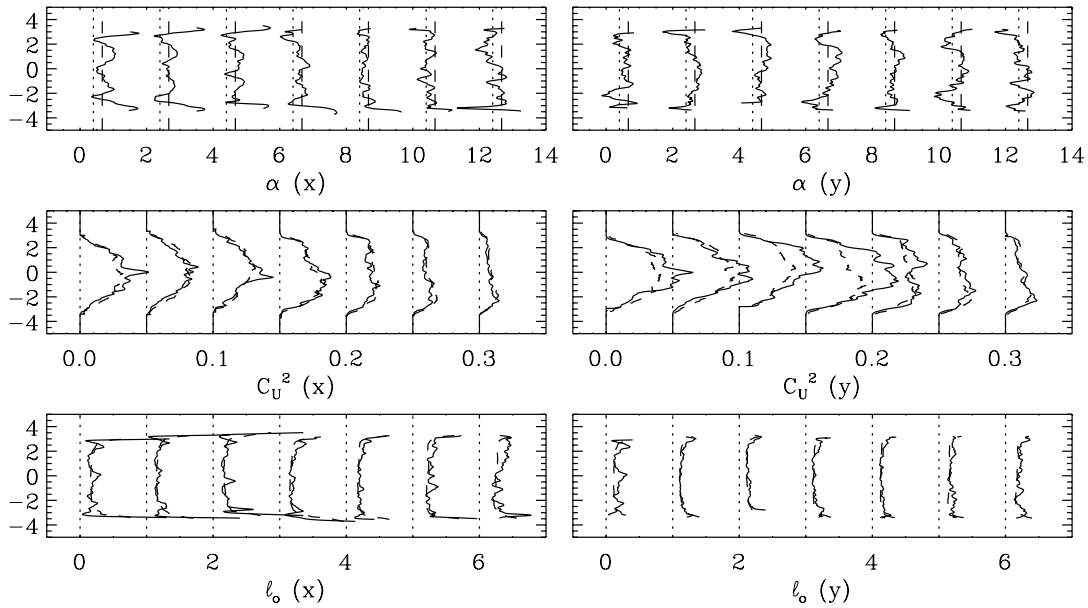


Figure 5: Profiles of streamwise-velocity structure-function fit parameters. See caption for Fig. 4 for details. In the middle row the dashed curve depicts $C_U^2 = C\epsilon^{2/3}$ for $r = x$ (left column) and $C_U^2 = 4/3C\epsilon^{2/3}$ for $r = y$ (right column) with the constant C chosen to be $C = 2.1$. C_ℓ is set to 11.3 for $r = x$ and 8.0 for $r = y$.

The determination of $C_\ell \approx 8.0$ from the transverse structure function of U is larger than that for the temperature. The value $C_\ell \approx 11.3$ obtained from the longitudinal structure function is larger than $C_\ell \approx 8.0$ by the factor $\sqrt{2}$. This increase in scale for ℓ_o for the longitudinal structure function is expected for isotropic turbulence, wherein $\langle \partial_y U \partial_y U \rangle = 2 \langle \partial_x U \partial_x U \rangle$, and hence, the smallest spatial scale in x for U should be larger than the smallest spatial scale in y by $\sqrt{2}$. Deviations from this isotropic result cannot be detected with the data presented in Fig. 5 as the natural variability of ℓ_o obtained from $\Delta_r U^2$ is apparently too large.

Figures similar to Figs. 4 and 5 for $\Delta_r V^2$ and $\Delta_r W^2$ have been computed, but are not shown here. The results share similarities with those already presented, but they also present differences. The major differences exhibited by $\Delta_r V^2$ and $\Delta_r W^2$ from $\Delta_r U^2$ are as follows: 1) α for W with $r = y$ is lower than for U , with nearly all values in the middle of the layer below $\alpha = 0.4$ for $t > 174$; 2) α for both V and W are significantly lower than $\alpha = 0.4$ (with $\alpha \approx 0.2$ to 0.3) for $r = x$; 3) $C \approx 0.9$ (1.6) for W (V); and 4) $C_\ell \approx 10.5$ (12.0) for W (V), again, with slightly larger values of C_ℓ for $r = x$ than for $r = y$. We note that values for $C \approx 1.6$ and $C \approx 0.9$ have been reported in the literature (Monin and Yaglom 1975), but further analysis is required to determine the significance of the results in our solutions.

Conclusions

The simulations presented exhibit large-scale flow dynamics which are approximately independent of Re (see Fig. 1), indicating that sufficiently high Re has likely been attained numerically to approximate similar processes as they appear in the atmosphere. Analysis

of the solutions demonstrate mean-flow/billow interactions that decay with time, eventually producing approximately stationary small-scale fluctuation dynamics for which production balances dissipation in the middle of the shear layer. Evaluation of universal constants C and C_θ and the structure function exponents α and the turbulence inner scale ℓ_o for temperature T and streamwise velocity U in the middle of the shear layer are in good agreement with atmospheric measurements, where available. Values for the parameters when obtained for the spanwise V and vertical velocity W , however, exhibit noteworthy differences from those obtained with U , indicating anisotropic influences of stratification and/or shear. Further work is required to understand these differences.

The edge regions of the shear layers remain challenging to characterize. The entrainment dynamics in the interface region between turbulent and quiescent fluid is observed to be non-stationary throughout the evolution of the layer. Previous results (Werne and Fritts 1999b) demonstrate this region to be highly anisotropic at small-scales in T . Because this region also exhibits the largest values of C_T^2 (see Fig. 4), it has the greatest impact on optical propagation. Nevertheless, despite the inherent difficulty in characterizing this region statistically, its impact on ABL design can be anticipated by combining these simulation results with results from in-situ and remote atmospheric observations.

This work is sponsored by AFRL F19628-98-C-0030, AFOSR F49620-98-C-0029, and ARO DAAD191-99-C-0037.

References

1. Brown, W.P., "Airborne Laser" 7th DoD HPC UGC, LaJolla, CA 1997.
2. Brown, W.P., "Optical Propagation Simulations for the Airborne Laser," HPCMO UGC, Ed. N. Sidki, Rice University, Houston, TX. June 1998, <http://www.hpcmo.hpc.mil/Htdocs/UGC/UGC98/papers/p5>
3. Brown, W.P., "Airborne Laser" 9th DoD HPC UGC, Monterey, CA 1999.
4. Bolgiano, R., "Turbulent Spectra in a Stably Stratified Atmosphere," J. Geophys. Res., Vol 64, pp.2226–2229, 1959.
5. Chilson, P.B., A.Muschinski and G.Schmidt, "First observations fo Kelvin-Helmholtz billows in an upper-level jet stream using VHF frequency domain interferometry," Radio Sci., Vol 32, 1997.
7. Ruster and Klostermeyer, Geophys. Astrophys. Fluid Dyn., Vol 26, 1983.
8. Coulman, C.E., J.Vernin and A.Fuchs, "Optical seeing-mechanism of formation of thin turbulent laminae in the atmosphere," Appl. Opt., Vol 34, pp.5461–5474, 1995.
9. Gibson, "Spectra of turbulence at high Re," Nature, Vol 195, pp.1281–1283, 1962.
10. Gibson, "Spectra of turbulence in a round jet," J. Fluid Mech., Vol 15, pp.161–173, 1963.
11. Gurvich, A.S., and S.L.Zubkovskii, "Estimate of the structure function of temperature fluctuation in the atmosphere," Izv. Akad. Nauk SSSR, Fiz. Atmosf. i Okeana, Vol 2, pp.202–204, 1966.

12. Hill, R.J., and S.F.Clifford, "Modified Spectrum of Atmospheric Temperature fluctuations and its Application to Opticla Propagation," J. Opt. Soc. Am., Vol 68, p.892, 1978.
13. Ierkic, H. M., R. F. Woodman and P. Perillat, "Ultrahigh vertical resolution radar measurements in the lower stratosphere at Arecibo," Radio Sci., Vol 25, pp.941-952, 1990.
14. Kaimal, J.C., J.C.Wyngaard, Y.Izumi and O.R.Coté, "Spectral characteristics of surface layer turbulence," Quart. J. Roy. Meteor. Soc., Vol 98, pp.305-317, 1972.
15. Kolmogorov, A.N., "Turbulence and stochastic processes: Kolmogorov's ideas 50 years on," eds. J.C.R. Hunt, O.M. Phillips and D. Williams, Proc.R. Soc.London, Ser. A 434, 1991. Page 9-13 The local structure of turbulence in incompressible viscous fluid for very large Reynolds numbers, Dokl.Akad.Nauk SSSR 30, 4, 1941. Page 15-17 Dissipation of energy in the locally isotropic turbulence, Dokl.Akad.Nauk SSSR 32, 1, 1941.
16. Monin, A. S. and A. M. Yaglom, "Statistical Fluid Mechanics, Vol 2" MIT Press, Cambridge, 1975.
17. Paquin, J.E., and S.Pond, "The determination of the Kolmogorov constants for velocity, temperature and humidity fluctuations from second- and third-order structure functions," J. Fluid Mech., Vol 50, pp.257-269, 1971.
18. Spalart, P.R., R.D.Moser and M.M.Rogers, "Spectral methods for the Navier-Stokes equations with one infinite and two periodic directions," J. Comput. Phys., Vol 96, pp.297-324, 1991.
19. Werne, J., P.Adams, and D.Sanders, "Linear scaling during production runs: conquering the I/O bottleneck," ARSC Cray T3E Users' Group Newsletter, <http://www.arsc.edu/pubs/T3Enews/T3Enews193.shtml>, March 31, 2000.
20. Werne, J., P.Adams, and D.Sanders, "Hierarchical Data Structure and Massively Parallel I/O," Parallel Computing, submitted, 2000.
21. Werne, J. and D.C.Fritts, "Turbulence in Stratified and Sheared Fluids: T3E Simulations" HPCMO UGC, Ed. N. Sidki, Rice University, Houston, TX. June 1998, http://www.hpcmo.hpc.mil/Htdocs/UGC/UGC98/papers/1f_chal
22. Werne, J. and D. C. Fritts, "Stratified shear turbulence: Evolution and Statistics" (cover article) Geophys. Res. Lett., Vol 26, pp.439-442, 1999a.
23. Werne, J. and D. C. Fritts, "Turbulence and Mixing in a Stratified Shear Layer: 3D K-H Simulations at $Re = 24,000$ " European Geophysical Society, XXIV General Assembly. April 1999, The Hague, 1999b.
24. Wyngaard, J.C., and O.R.Coté, "The budgets of turbulent kinetic energy and temperature variance in the atmosphere surface layer," J. Atmos. Sci., Vol 28, pp.190-201.
25. Wyngaard, J.C., and Y.H.Pao, "Some measurements of the fine structure of large Reynolds number turbulence. *Statistical Models and Turbulence. Proceedings of the Symposium at San Diego, July 15-21, 1971* (M.Rosenblatt and C.Van Atta, eds.), Lecture Notes in Physics, Springer-Verlag, Berlin-Heidelberg-New York.